Supplementary Information (SI) for Nanoscale.

Rationalizing high-entropy catalytic self-Fenton pollutant degradation from an effective porous piezoelectric composite film

Jiahui Cai, Feng Han*, Dan Tian, Xinnan Li, Jialin Zhuang, Yunfan Chen, and Qi An*.

J. Cai, F. Han, X. Li, J. Zhuang, Y. Chen, Q. An
School of Materials Science and Technology
China University of Geosciences (Beijing)
No.29 Xueyuan Road, Hai Dian District
Beijing 100083, P. R. China
E-mail: hanfeng@cugb.edu.cn (F. Han), an@cugb.edu.cn (Q. An)

D. Tian
CanFit Resource Technologies Inc.
No.65 Fushi Road, Hai Dian District
Beijing 100143, P. R. China

Supporting Information

Text captions:

Text S1 Chemicals used in this study.
Text S2 Characterizations.
Text S3 Detailed steps of the reactive oxygen species (ROS) quantification assay experiment.
Text S4 About the choice of the MgO@rGO/PVDF-HFP as the matrix.
Text S5 The possible reason for the high adsorption rates for MB on Fe and FeC_2O_4 nanoparticles.
Text S6 Detailed steps for electrochemical correlation test.
Text S7 Detailed steps of the quantitative total iron concentration assay experiment.
Text S8 The reusability of the composite films.

Figure captions:

Figure S1 Comparison of degradation rates of various dyes using composite films doped with different iron sources.
Figure S2 Comparison of ROS production concentrations in composite films doped with different iron sources.
Figure S3 Redox potential corrected according to the Nernst equation.
Figure S4 Total redox potential corrected for the pH of the reaction environment.
Figure S5 ATR-IR spectra of each composite film.
Figure S6 Comparison of various properties of different iron sources and doped composite films.
Figure S7 UV-visible absorbance curves for degradation of mixed dyes during a degradation period of 60 min.
Figure S8 SEM and EDS mapping image of fillers. SEM image of composite cross-section.
Figure S9 SEM and EDS mapping images of the composite film after the chloroplatinic acid deposition experiments.
Figure S10 Leached total iron concentrations during composite film catalysis.
Figure S11 Cycling performance of composite films.

Text S1 Chemicals used in this study

Magnesium oxide (MgO, 99.8%), ferric oxide (Fe_2O_3, 99.5%), glacial acetic acid (CH_3COOH, 99.8%), terephthalic acid (TA, $C_8H_6O_4$, AR), nitrotetrazolium blue chloride (NBT, $C_{40}H_{30}Cl_2N_{10}O_6$, 98%), hydrogen peroxide (H_2O_2, AR, 30 wt.% in H_2O), sodium sulfate anhydrous (Na_2SO_4, AR) were purchased from Aladdin. N,N-dimethylacetamide (DMAC, C_4H_9NO, 99%), iron nanopowder (Fe, 99.9%), ferric tetraoxide (Fe_3O_4, 99.5%), ferrous disulfide (FeS_2, 99.9%), ferric phosphate ($FePO_4$, 98%), ferrous oxalate (FeC_2O_4, Fe>30.5%), methylene blue (MB. $C_{16}H_{18}N_3ClS$, AR), anhydrous sodium acetate (CH_3COONa, 99.9%), horseradish peroxidase (HRP, 95%), 3,3',5,5'-tetramethylbenzidine (TMB, $C_{16}H_{20}N_2$, 98%), dimethylsulfoxide (DMSO, C_2H_6OS, AR), cloroplantinic acid (H_2PtCl_6, 8 wt.%) in H_2O), hydroxylamine hydrochloride ($HONH_2HCl$, 99%), ethyl cellulose (($C_{12}H_{22}O_5$)n) were purchased from Macklin. Methyl orange (MO, $C_{14}H_{14}N_3SO_3Na$, AR) and hydrochloric acid (HCl, AR) were purchased from Beijing Chemical Factory. Polyvinylidene fluoride-hexafluoropropylene (PVDF-HFP, $(-CH_2CF_2-)_x[-CF_2CF(CF_3)-]_y$, 1.78 g/cm^3, 5-20% HFP content) was purchased from Sigma-Aldrich. Reduced graphene oxide (rGO, Single layer ratio 80%) was purchased from Jiangsu Xianfeng Nanomaterials Technology Co. Iron phthalocyanine (FePc, $C_{32}H_{16}FeN_8$, 96%) was purchased from Acros Organics. Rhodamine B (RhB, $C_{28}H_{31}ClN_2O_3$, AR) was purchased from Sinopharm Chemical Reagent Co. Sodium hydroxide (NaOH, AR) was purchased from Beijing Yili Fine Chemicals Co. o-Phenanthroline ($C_{12}H_8N_2$, 99%) was purchased from Tianjin Beichen Fangzheng Reagent Factory. Ethanol anhydrous (CH_3CH_2OH, AR) was purchased from Tangshan Zhongxu Shengjin Trading Co.

Text S2 Characterizations

Attenuated total reflectance-IR (ATR-IR, Bruker, TENSOR II) was used to quantify the β-phase content of each PVDF-HFP composite film. Nanoparticle size and zeta potential analyzer (Malvern Panalytical, Nano-ZS90) and Automatic specific surface and porosity analyzer (BET, Micromeritics Tristar II 3020) was used to measure the zeta potential and specific surface area of each doped powder in the composite film. Scanning electron microscopy (SEM) and energy dispersive X-ray spectroscopy (EDS) (ZEISS, Sigma 360) were used for surface and cross-sectional morphological characterization of the composite films as well as for the surface elemental distribution. X-ray photoelectron spectroscopy (XPS, Thermo Scientific, K-Alpha) was employed to analyze the valence distribution of elemental Fe on the surface of Fe nanopowder and to probe the effects of H_2O_2 and piezocatalysis on the redox process of Fe on the surface of the composite film.

Text S3 Detailed steps of the reactive oxygen species (ROS) quantification assay experiment

Hydrogen peroxide (H_2O_2):

For quantitative detection of H_2O_2, 3,3',5,5'-Tetramethylbenzidine (TMB) colorimetric spectrophotometry was used. Prior to the experiment, a 0.2 mol/L buffer solution (prepared from anhydrous sodium acetate and glacial acetic acid), a 0.1 mg/mL aqueous HRP solution, and a 10 mg/mL TMB solution (dissolved in DMSO) were prepared. The experiment involved adding 10 mL of deionized water and 0.05 g of the catalyst to a 25 mL beaker. The ultrasonic cleaner (Supmile, KQ-300DE) was activated to start the experiment. At specified time intervals, 500 μL of the solution sample was collected, and 1.8 mL of buffer solution, 100 μL of HRP solution, and 100 μL of TMB solution were added sequentially. After thorough mixing, the solution was allowed to stand for 10 minutes. The UV-visible absorption spectrum (Shimadzu, UV-2600) was measured once the solution was sufficiently colored, with a peak observed near 652 nm.

Hydroxyl radical ($\cdot OH$):

For quantitative detection of $\cdot OH$, the terephthalic acid (TA) fluorescent probe method was employed. Prior to the experiment, an aqueous 0.5 μmol/L TA solution was prepared, with an equal amount of NaOH added to promote TA dissolution. For the experiment, 10 mL of the TA solution and 0.05 g of the catalyst were placed in a 25 mL beaker. The experiment commenced by activating the ultrasonic cleaner. A 4 mL sample of the solution was collected at specified time intervals, and the fluorescence spectrum (Lengguang Technology, F97XP) was measured, with the peak observed near 425 nm. After each measurement, the sample was returned to the beaker for the next ultrasonication period.

Superoxide radical ($\cdot O_2^-$):

For the quantitative detection of $\cdot O_2^-$, the nitrotetrazolium blue chloride (NBT) conversion spectrophotometric method was employed. An aqueous 0.025 mol/L NBT solution was prepared before the experiment. For the procedure, 10 mL of the NBT solution and 0.05 g of the catalyst were placed in a 25 mL beaker. The experiment commenced with the activation of the ultrasonic cleaner. A 4 mL sample of the solution was collected at specific time intervals, and the UV-visible absorption spectrum was measured, with the peak observed near 259 nm. After each measurement, the solution sample was returned to the beaker for the next ultrasonication period.

Text S4 About the choice of the MgO@rGO/PVDF-HFP as the matrix.

MgO@rGO/PVDF-HFP is chosen as the matrix to further incorporate iron sources for the following reasons.

Firstly, for the MgO nanoparticles in the catalyst system, they act as crystalline nuclei within the PVDF-HFP matrix. This helps increase the β-phase content, thereby improving the piezoelectric output performance of the films[1,2]. Additionally, based on our data regarding the ROS concentration produced by the MgO@rGO/PVDF-HFP composite film, which exhibits a high H_2O_2 yield, we hypothesize that MgO provides abundant active sites for H_2O_2 production, thereby enhancing the efficiency of dissolved oxygen utilization in the catalytic process. In our control experiments, the MgO-doped composite films exhibited a 13.09% improvement in RhB degradation performance compared to the undoped Fe_3O_4@rGO/PVDF-HFP films.

Secondly, rGO plays two key roles in the catalyst system. First, its ultra-high specific surface area facilitates the aggregation of reactants on the catalyst surface[3]. Additionally, other powder materials doped into the catalyst system are supported on the sheet-like structure of rGO, which reduces the mass transfer distance between reactant molecules and catalyst components, thereby enhancing catalytic efficiency. Second, rGO enhances carrier migration due to its excellent conductivity, which accelerates carrier movement among the catalyst components, thereby boosting catalytic activity[3,4]. In our control experiments, the rGO-doped composite film demonstrated a 148.14% improvement in RhB degradation performance compared to the undoped MgO@Fe_3O_4/PVDF-HFP film.

Text S5 The possible reason for the high adsorption rates for MB on Fe and FeC_2O_4 nanoparticles.

Despite the positive surface charge of Fe and FeC_2O_4, their high adsorption rates for MB may be attributed to the following mechanisms.

First, the zeta potential in this experiment was measured by dispersing the filler in deionized water[5–7]. Both the solution pH and ionic strength are important factors influencing the zeta potential. The weak alkalinity of the MB solution, along with the presence of chloride ions (Cl^-), may partially shield the material's surface charge, thereby reducing the repulsive effect of the positively charged surface on cationic dyes.

Second, the surface characteristics of the adsorbent play a crucial role in the surface adsorption process[8,9]. For instance, Fe and FeC_2O_4 surfaces typically contain a large number of lattice defects and active sites, which can trap MB molecules through physical adsorption or chemical interactions.

Finally, the structural properties of the adsorbent also significantly influence its adsorption performance[6,10]. For instance, MB molecules may overcome electrostatic repulsion via coordination or hydrogen bonding interactions with the Fe and FeC_2O_4 surfaces, facilitated by the aromatic rings or functional groups present in the MB molecules.

Text S6 Detailed steps for electrochemical correlation test

A CHI 760E electrochemical workstation was used to measure the electrochemical impedance spectroscopy (EIS) and linear scan voltammetry (LSV) curves of each iron source-doped powder in the composite film. All experiments were conducted at room temperature. The iron source, Ag/AgCl (saturated KCl), and Pt wire served as the working, reference, and counter electrodes, respectively. The iron source powder was coated onto ITO glass with a 2×3 cm area, and a 0.1 M Na_2SO_4 aqueous solution was used as the electrolyte. To enhance catalyst adhesion to the ITO substrate, ethyl cellulose was used as a binder. A suspension was prepared by dispersing 10 mg of iron source powder in 1 mL of ethyl cellulose solution (1 mg/mL in anhydrous ethanol). The solution was then coated onto the ITO glass and allowed to dry.

Text S7 Detailed steps of the quantitative total iron concentration assay experiment

A modified o-phenanthroline colorimetric spectrophotometric method was employed for the quantitative determination of total iron concentration. Prior to the experiment, 100 g/L aqueous hydroxylamine hydrochloride, 10 wt.% aqueous sodium acetate, and 2 g/L aqueous o-phenanthroline solutions were prepared. For the procedure, 10 mL of deionized water and 0.05 g of catalyst were added to a 25 mL beaker. The experiment commenced with the activation of the ultrasonic cleaner, after which a 500 μL sample of the solution was collected at specific intervals. Subsequently, 500 μL of hydroxylamine hydrochloride solution, 1 mL of sodium acetate solution, and 1 mL of o-phenanthroline solution were sequentially added. The mixture was stirred thoroughly and allowed to stand for 5 minutes. The UV-visible absorption spectrum was then measured after sufficient color development, with the absorption peak near 510 nm.

Text S8 The reusability of the composite films.

MB was selected as the model dye to facilitate degradation rate calculations, and the results are presented in revised Figure S11. The data show that the composite film maintained a high degradation rate across four consecutive cycles, achieving degradation efficiencies of 81.31%, 82.40%, 70.47%, and 61.42%, respectively. However, a more significant performance decline was observed in the fifth cycle, where the degradation rate dropped to 48.51%.

These results indicate that the composite film exhibits a certain degree of cycling stability. The loss of degradation performance over repeated use may stem from the dissolution of iron ions and passivation of the surface layers. However, considering its simple preparation process and easy recyclability, the catalysts may subject to regeneration processes, which requires further studies.

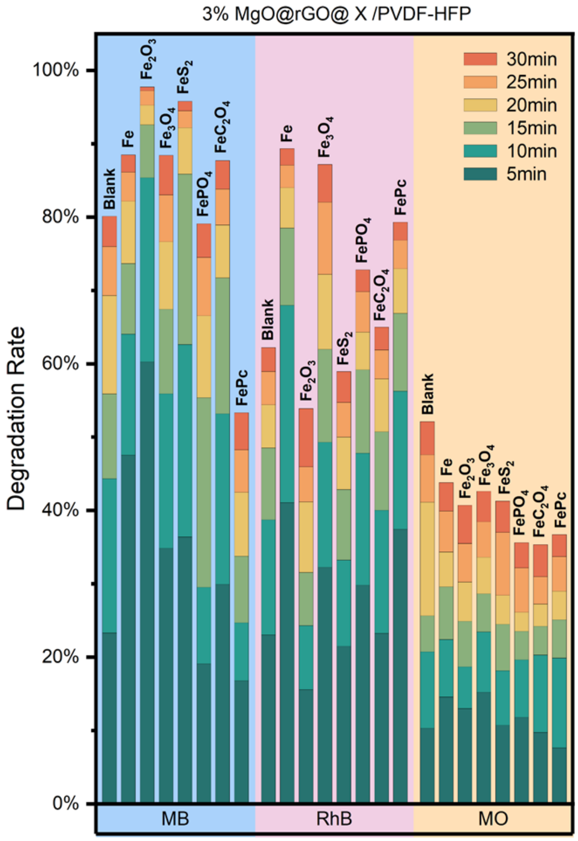

Figure S1 Comparison of degradation rates of various dyes using composite films doped with different iron sources.

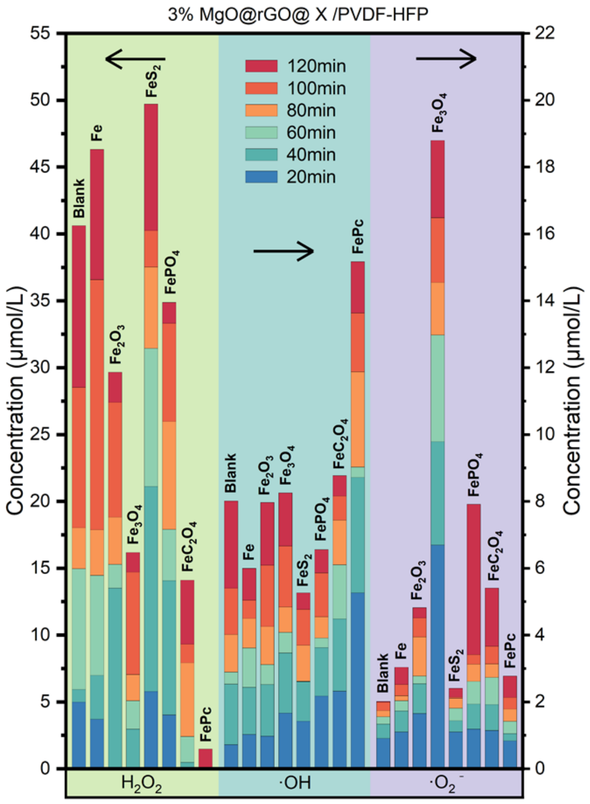

Figure S2 Comparison of ROS production concentrations in composite films doped with different iron sources.

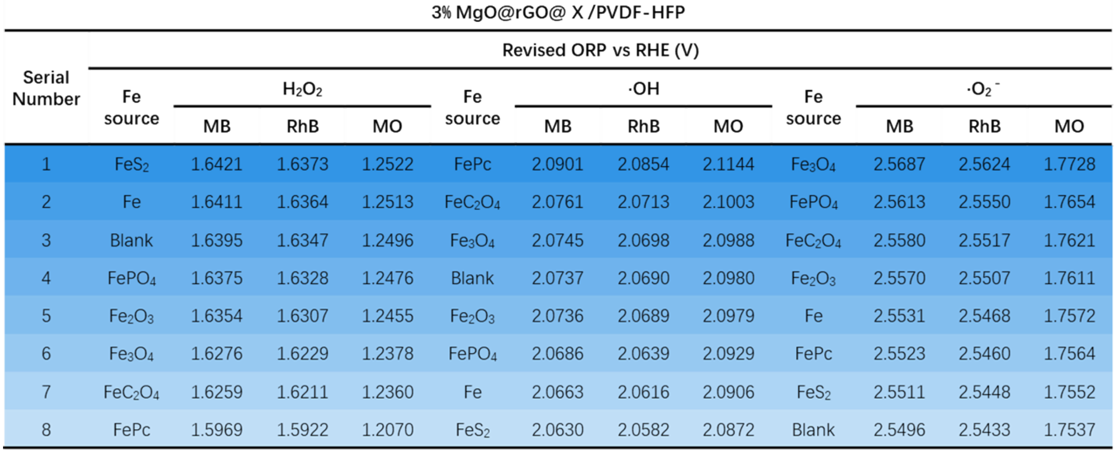

3% MgO@rGO@ X /PVDF-HFP

Serial Number	Revised ORP vs RHE (V)											
	Fe source	H_2O_2			Fe source	$\cdot OH$			Fe source	$\cdot O_2^-$		
		MB	RhB	MO		MB	RhB	MO		MB	RhB	MO
1	FeS_2	1.6421	1.6373	1.2522	FePc	2.0901	2.0854	2.1144	Fe_3O_4	2.5687	2.5624	1.7728
2	Fe	1.6411	1.6364	1.2513	FeC_2O_4	2.0761	2.0713	2.1003	$FePO_4$	2.5613	2.5550	1.7654
3	Blank	1.6395	1.6347	1.2496	Fe_3O_4	2.0745	2.0698	2.0988	FeC_2O_4	2.5580	2.5517	1.7621
4	$FePO_4$	1.6375	1.6328	1.2476	Blank	2.0737	2.0690	2.0980	Fe_2O_3	2.5570	2.5507	1.7611
5	Fe_2O_3	1.6354	1.6307	1.2455	Fe_2O_3	2.0736	2.0689	2.0979	Fe	2.5531	2.5468	1.7572
6	Fe_3O_4	1.6276	1.6229	1.2378	$FePO_4$	2.0686	2.0639	2.0929	FePc	2.5523	2.5460	1.7564
7	FeC_2O_4	1.6259	1.6211	1.2360	Fe	2.0663	2.0616	2.0906	FeS_2	2.5511	2.5448	1.7552
8	FePc	1.5969	1.5922	1.2070	FeS_2	2.0630	2.0582	2.0872	Blank	2.5496	2.5433	1.7537

Figure S3 Redox potential corrected according to the Nernst equation.

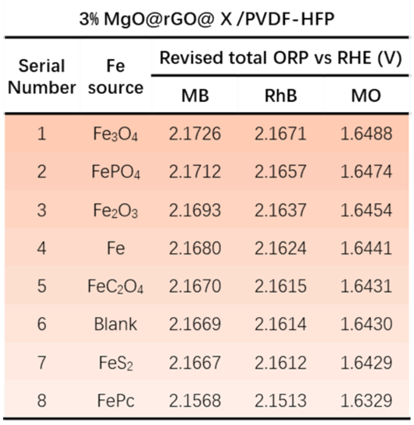

3% MgO@rGO@ X /PVDF-HFP

Serial Number	Fe source	Revised total ORP vs RHE (V)		
		MB	RhB	MO
1	Fe_3O_4	2.1726	2.1671	1.6488
2	$FePO_4$	2.1712	2.1657	1.6474
3	Fe_2O_3	2.1693	2.1637	1.6454
4	Fe	2.1680	2.1624	1.6441
5	FeC_2O_4	2.1670	2.1615	1.6431
6	Blank	2.1669	2.1614	1.6430
7	FeS_2	2.1667	2.1612	1.6429
8	FePc	2.1568	2.1513	1.6329

Figure S4 Total redox potential corrected for the pH of the reaction environment.

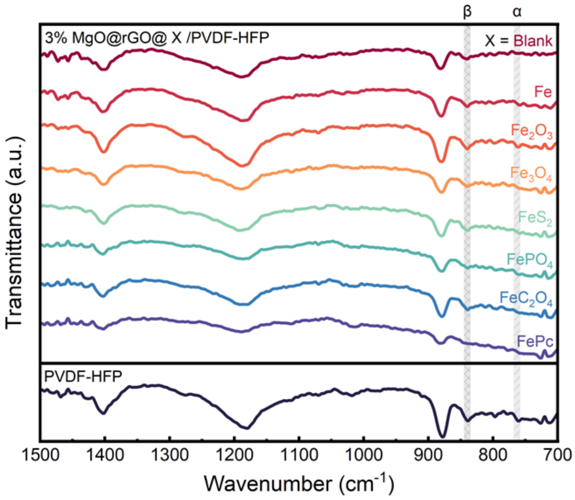

Figure S5 ATR-IR spectra of each composite film.

Composite film performance: 3% MgO@rGO@ X /PVDF-HFP

Pollutants	Performance		Fe source						
			Fe	Fe_2O_3	Fe_3O_4	FeS_2	$FePO_4$	FeC_2O_4	FePc
MB	Degradation Rate		0.79	1.00	0.79	0.96	0.58	0.77	0.00
	Revised ORP vs RHE	H_2O_2	0.98	0.85	0.68	1.00	0.90	0.64	0.00
		•OH	0.12	0.39	0.43	0.00	0.21	0.48	1.00
		$•O_2^-$	0.11	0.34	1.00	0.00	0.58	0.39	0.07
		Total	0.71	0.79	1.00	0.63	0.91	0.64	0.00
RhB	Degradation Rate		1.00	0.00	0.94	0.14	0.53	0.31	0.72
	Revised ORP vs RHE	H_2O_2	0.98	0.85	0.68	1.00	0.90	0.64	0.00
		•OH	0.12	0.39	0.43	0.00	0.21	0.48	1.00
		$•O_2^-$	0.11	0.34	1.00	0.00	0.58	0.39	0.07
		Total	0.71	0.79	1.00	0.63	0.91	0.64	0.00
MO	Degradation Rate		1.00	0.63	0.86	0.70	0.03	0.00	0.16
	Revised ORP vs RHE	H_2O_2	0.98	0.85	0.68	1.00	0.90	0.64	0.00
		•OH	0.12	0.39	0.43	0.00	0.21	0.48	1.00
		$•O_2^-$	0.11	0.34	1.00	0.00	0.58	0.39	0.07
		Total	0.71	0.79	1.00	0.63	0.91	0.64	0.00

Fe source performance

Performance	Fe source						
	Fe	Fe_2O_3	Fe_3O_4	FeS_2	$FePO_4$	FeC_2O_4	FePc
MB Adsorption Rate	1.00	0.28	0.59	0.25	0.00	0.74	0.00
RhB Adsorption Rate	0.64	0.46	0.92	0.62	0.37	1.00	0.00
MO Adsorption Rate	0.93	0.14	0.18	1.00	0.31	0.58	0.00
Surface Area (BET)	0.10	0.63	1.00	0.00	0.04	0.02	0.00
Redox Current (LSV)	0.26	0.33	1.00	0.41	0.00	0.92	0.11
Interfacial Charge Transfer Resistance (EIS)	1st	2nd	3rd	5th	7th	4th	6th

Figure S6 Comparison of various properties of different iron sources and doped composite films.

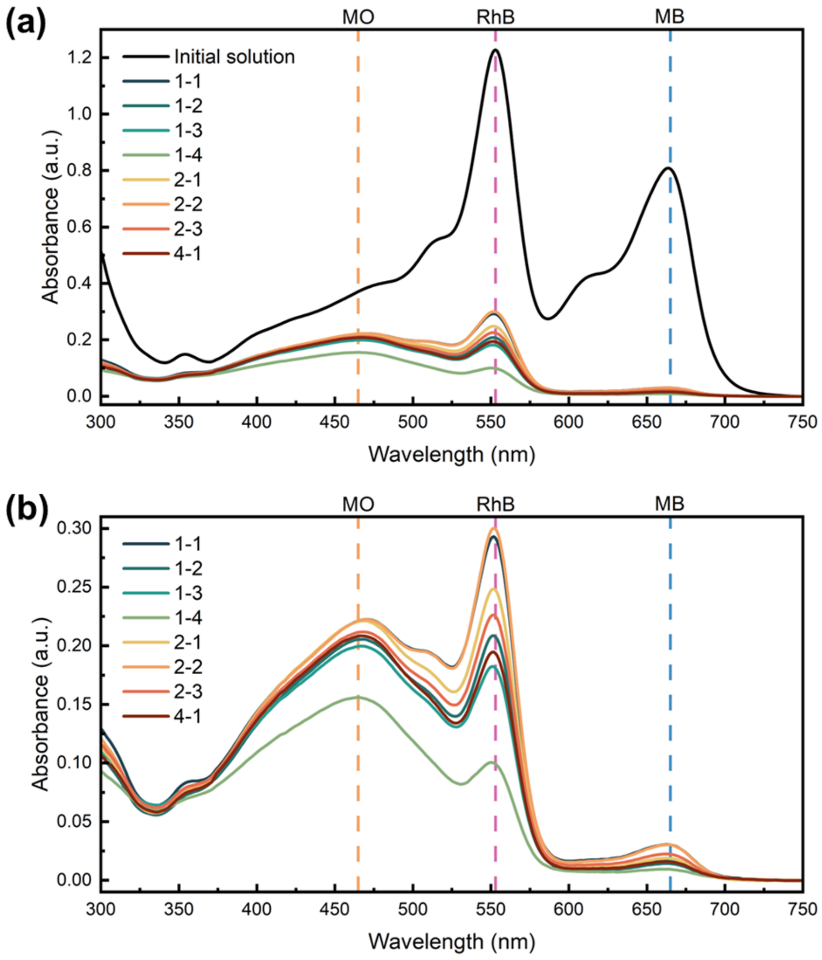

Figure S7 (a) UV-visible absorbance curve and (b) local magnification of the degradation of mixed dyes during a degradation period of 60 min.

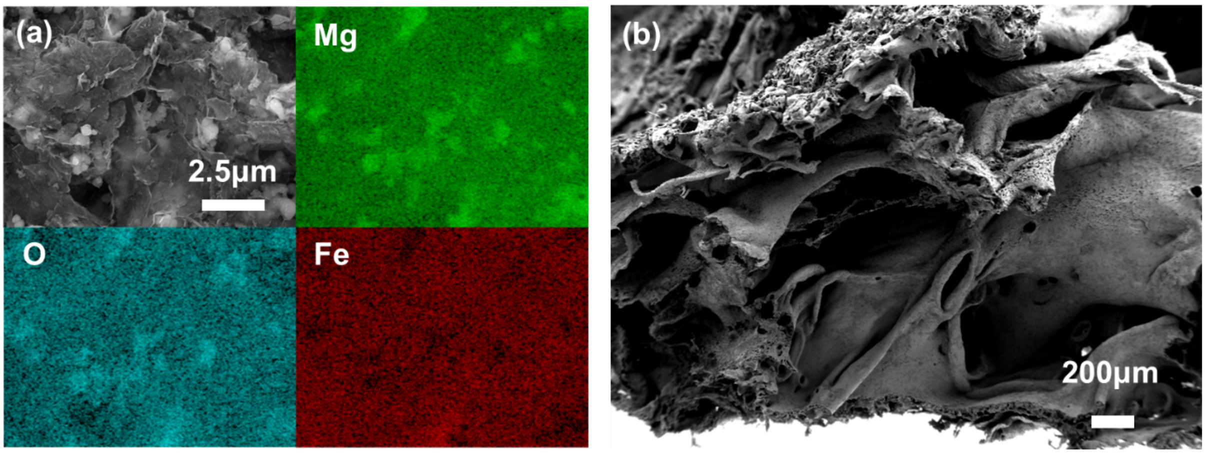

Figure S8 (a) SEM and EDS mapping image of fillers. (b) SEM image of composite cross-section.

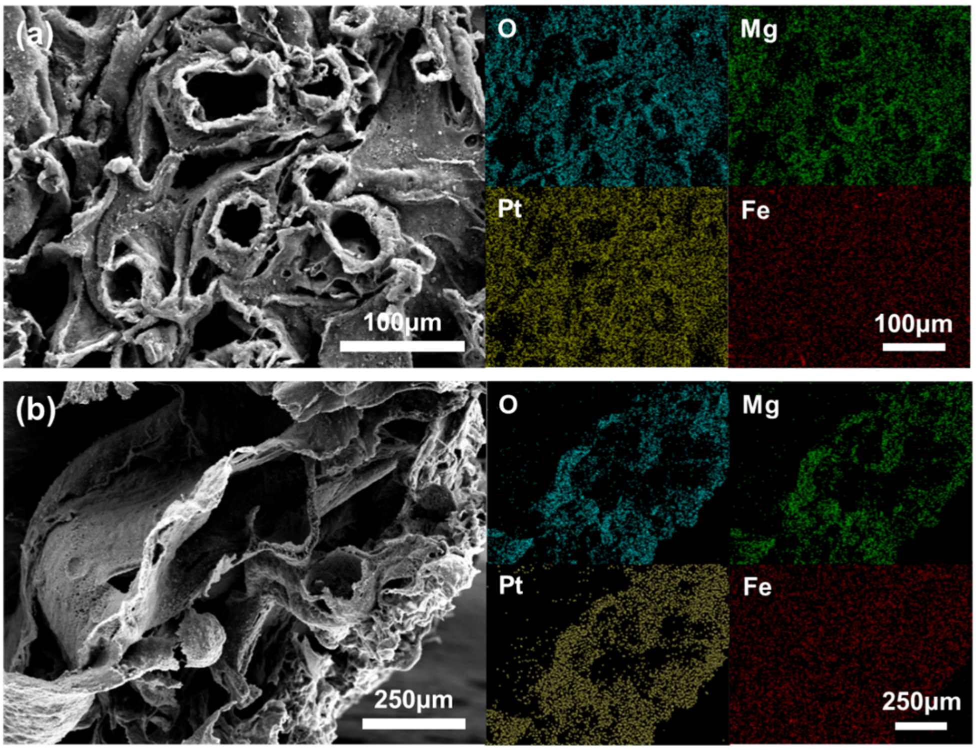

Figure S9 SEM and EDS mapping images of (a) the composite film surface and (b) cross-section after the chloroplatinic acid deposition experiment.

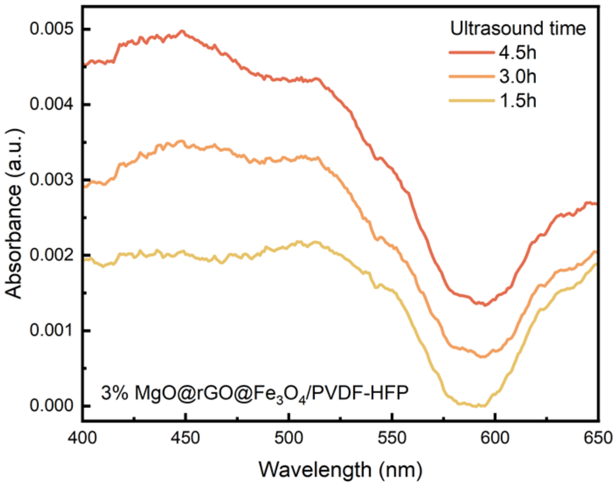

Figure S10 UV-visible absorbance curves determined by the modified o-phenanthroline method.

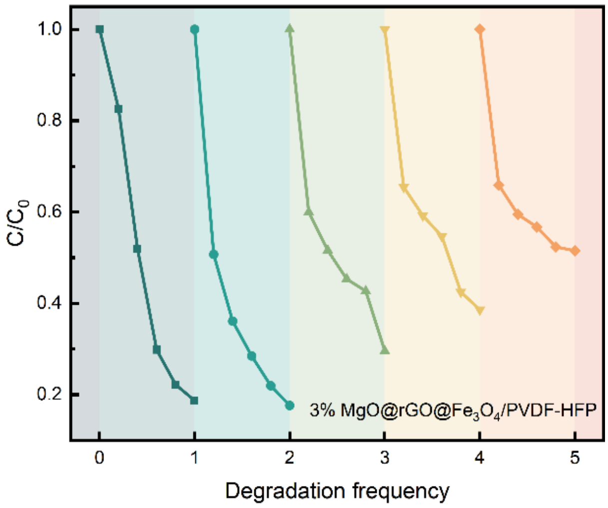

Figure S11 Cycling performance of composite films.

References

1 L. Wan, W. Tian, N. Li, D. Chen, Q. Xu, H. Li, J. He and J. Lu, *Nano Energy*, 2022, **94**, 106930.

2 S. S. Nardekar, K. Krishnamoorthy, P. Pazhamalai, S. Sahoo and S. Jae Kim, *Nano Energy*, 2022, **93**, 106869.

3 L. Lyu, G. Yu, L. Zhang, C. Hu and Y. Sun, *Environ. Sci. Technol.*, 2018, **52**, 747–756.

4 S. G. Babu, Ramalingam Vinoth, B. Neppolian, D. D. Dionysiou and M. Ashokkumar, *Journal of Hazardous Materials*, 2015, **291**, 83–92.

5 Z. Kang, N. Qin, E. Lin, J. Wu, B. Yuan and D. Bao, *Journal of Cleaner Production*, 2020, **261**, 121125.

6 Q. Huang, S. Jin, S. Song and Z. Chen, *Journal of Cleaner Production*, 2022, **363**, 132604.

7 A. Gordanshekan, S. Arabian, A. R. Solaimany Nazar, M. Farhadian and S. Tangestaninejad, *Chemical Engineering Journal*, 2023, **451**, 139067.

8 D.-M. Liu, J.-T. Zhang, C.-C. Jin, B.-B. Chen, J. Hu, R. Zhu and F. Wang, *Nano Energy*, 2022, **95**, 106975.

9 Y. Du, T. Lu, X. Li, Y. Liu, W. Sun, S. Zhang and Z. Cheng, *Nano Energy*, 2022, **104**, 107919.

10 J. Wu, B. Li, Y. Shao, X. Wu and W. Zhao, *Environ Chem Lett*, 2020, **18**, 2141–2148.